Monthly Notices
of the
ROYAL ASTRONOMICAL SOCIETY

MNRAS **475,** 5501–5512 (2018)
Advance Access publication 2018 January 23

doi:10.1093/mnras/sty180

A search for cyanopolyynes in L1157-B1

Edgar Mendoza,[1,2★] B. Lefloch,[1,2★] C. Ceccarelli,[2] C. Kahane,[2] A. A. Jaber,[2,3] L. Podio,[4] M. Benedettini,[5] C. Codella,[4] S. Viti,[6] I. Jimenez-Serra,[7] J. R. D. Lepine,[1] H. M. Boechat-Roberty[8] and R. Bachiller[9]

[1]*Instituto de Astronomia, Geofísica e Ciências Atmosféricas, Universidade de São Paulo, São Paulo 05508-090, SP, Brazil*
[2]*Univ. Grenoble Alpes, CNRS, IPAG, F-38000 Grenoble, France*
[3]*University of AL-Muthanna, College of Science, Physics Department, AL-Muthanna, Iraq*
[4]*INAF, Osservatorio Astrofisico di Arcetri, Largo Enrico Fermi 5, I-50125 Firenze, Italy*
[5]*INAF, Istituto di Astrofisica e Planetologia Spaziali, via Fosso del Cavaliere 100, I-00133 Roma, Italy*
[6]*Department of Physics and Astronomy, University College London, Gower Street, London WC1E 6BT, England*
[7]*School of Physics and Astronomy, Queen Mary, University of London, Mile End Road, London E1 4NS, England*
[8]*Observatório do Valongo, Universidade Federal do Rio de Janeiro - UFRJ, Rio de Janeiro 20080-090, RJ, Brazil*
[9]*IGN, Observatorio Astronómico Nacional, Calle Alfonso XII, 3 E-28004 Madrid, Spain*

Accepted 2018 January 5. Received 2017 November 7; in original form 2017 September 12

ABSTRACT

We present here a systematic search for cyanopolyynes in the shock region L1157-B1 and its associated protostar L1157-mm in the framework of the Large Program 'Astrochemical Surveys At IRAM' (ASAI), dedicated to chemical surveys of solar-type star-forming regions with the IRAM 30-m telescope. Observations of the millimeter windows between 72 and 272 GHz permitted the detection of HC_3N and its 13C isotopologues, and HC_5N (for the first time in a protostellar shock region). In the shock, the analysis of the line profiles shows that the emission arises from the outflow cavities associated with L1157-B1 and L1157-B2. Molecular abundances and excitation conditions were obtained from the analysis of the Spectral Line Energy Distributions under the assumption of Local Thermodynamical Equilibrium or using a radiative transfer code in the Large Velocity Gradient approximation. Towards L1157 mm, the HC_3N emission arises from the cold envelope ($T_{rot} = 10$ K) and a higher-excitation region ($T_{rot} = 31$ K) of smaller extent around the protostar. We did not find any evidence of ^{13}C or D fractionation enrichment towards L1157-B1. We obtain a relative abundance ratio HC_3N/HC_5N of 3.3 in the shocked gas. We find an increase by a factor of 30 of the HC_3N abundance between the envelope of L1157-mm and the shock region itself. Altogether, these results are consistent with a scenario in which the bulk of HC_3N was produced by means of gas phase reactions in the passage of the shock. This scenario is supported by the predictions of a parametric shock code coupled with the chemical model UCL_CHEM.

Key words: astrochemistry – stars: formation – ISM: abundances – ISM: jets and outflows – ISM: molecules.

1 INTRODUCTION

Cyanopolyynes ($HC_{2n+1}N$) are molecules found in a wide range of environments in our Galaxy, from comets in our Solar system (Crovisier et al. 2004) to molecular clouds (Takano et al. 1998, 2014) and evolved stars (Cernicharo & Guélin 1996). In star-forming regions, only relatively short chains have been reported in the literature so far, up to $HC_{11}N$, in dense cold cores (Bell et al. 1997) and hydrocarbon-rich protostellar envelopes of low-mass (WCCC) sources (e.g. Sakai et al. 2008; Cordiner et al. 2012; Friesen et al. 2013).

An important property of cyanopolyynes is their stability against strong radiation field and cosmic rays (Clarke & Ferris 1995). Recently, Jaber Al-Edhari et al. (2017) showed how the cyanopolyyne emission properties could be used to trace the history of the IRAS16293−2422 protostellar envelope.

The presence of cyanopolyynes in protostellar shock regions has received relatively little attention since the detection of HC_3N by Bachiller & Perez-Gutíerrez (1997) in the outflow shocks of L1157, a low-mass star-forming region at ∼250 pc (Looney, Tobin & Kwon 2007). They estimated an increase of the molecular abundance by about 2 orders of magnitude between the outflow shock regions

★ E-mail: emendoza@usp.br (EM); Bertrand.Lefloch@univ-grenoble-alpes.fr (BL)

L1157-B1/B2 and the position of the protostar L1157-mm. Their estimate was based on a simple LTE analysis of three transitions only. No evidence for more complex cyanopolyyne (HC_5N) was found. The survey of L1157-B1 in the 3mm window with the 45-m telescope of the Nobeyama Radio Observatory by Yamaguchi et al. (2012) only confirmed the above results, and no substantial advances were made in the chemistry of cyanopolyynes and the presence of longer chains.

The outflow shock region L1157-B1 and the outflow driving protostar L1157-mm have been the subject of a thorough study by our team, in particular as part of the observational Large Program 'Astrochemical Surveys At IRAM' (ASAI;[1] Lefloch et al. 2017a) with the IRAM 30-m telescope. These various studies have provided us with a unique data set, which offers the possibility of investigating the physical and chemical structure of a typical protostellar shock (Codella et al. 2010, Codella et al. 2012, 2015, 2017; Lefloch et al. 2010, 2012, 2016, 2017b; Benedettini et al. 2012, 2013; Busquet et al. 2014; Podio et al. 2014, 2016, 2017).

In this work, we present an observational study on the chemistry of cyanopolyynes, in a shock region, as well as the impact of protostellar shock on the chemical conditions in the ambient cloud. The paper is organized as follows. In Section 2, we summarize the main observational properties of the shock region L1157-B1. The observations are described in Section 3. In Section 4, we present the molecular transitions of cyanopolyynes detected in the ASAI line survey. The properties of the shock, the origin of the emission, and the shock physical conditions (density, temperature, abundance) are discussed in Section 5. The cyanopolyyne emission towards the protostar is presented in Section 6. We discuss our results in Section 7. Finally, we present our conclusions in Section 8.

2 THE L1157-B1 SHOCK REGION

The L1157 bipolar and chemically rich molecular outflow (Bachiller et al. 2001) is swept up by an episodic and precessing jet (Gueth, Guilloteau & Bachiller 1996, 1998; Tafalla et al. 2015; Podio et al. 2016) driven by the L1157-mm Class 0 protostar. The blue-shifted southern lobe mainly consists of two main cavities with different kinematical ages: B1 (≈1100 yr), and the older and more extended B2 (1800 yr). The bright bow shock at the B1 cavity is located at ∼ 69 arcsec (0.1 pc) from the protostar (see Fig. 1), and various molecular tracers indicate warm shocked gas enriched by the injection of dust mantle and core products, such as CH_3OH, NH_3, H_2CO, NH_2CHO (see e.g. Tafalla & Bachiller 1995; Codella et al. 2010, Codella et al. 2017; Benedettini et al. 2012; Mendoza et al. 2014; Lefloch et al. 2017b; and references therein). High-angular resolution observations of these tracers with the Plateau de Bure Interferometer (PdBI) reveal the presence of a few high-velocity clumps (B1a-b-c and B0e) whereas the lower velocity material traces the expansion of the cavity excavated by the shock (see e.g. Benedettini et al. 2013).

Previous analysis of the CO and CS gas kinematics, as observed with the IRAM 30-m telescope (Lefloch et al. 2012; Gómez-Ruiz et al. 2015), has led to identify three physically distinct components coexisting in L1157-B1, labelled as follows and summarized in Table 1:

(i) g_1: the region of ∼7–10 arcsec at $T_{\rm kin} \sim 210$ K and $n_{\rm H_2} \geq 10^6$ cm^{-3}, associated with a dissociative *J*-shock due to the youngest impact of the jet against the B1 cavity walls.

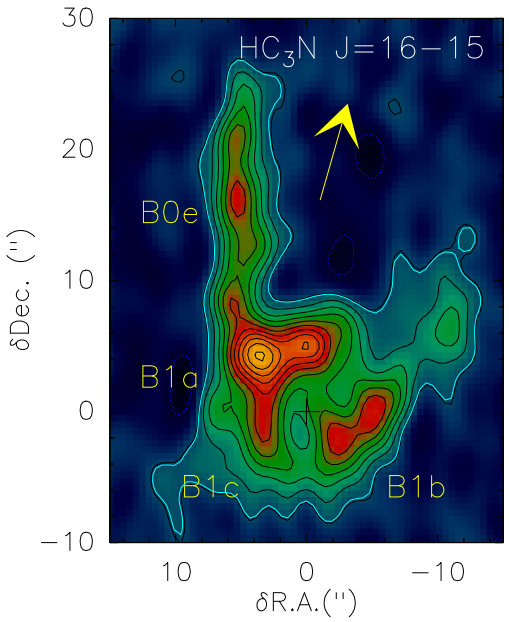

Figure 1. The L1157-B1 bow-shock region as traced by the HC_3N(16–15) emission, observed with the PdB interferometer (from Benedettini et al. 2013). The location of the individual shocked clumps B1a-b-c and B0e indicated (Benedettini et al. 2013). The arrow points to the direction of the L1157-mm protostar. The first contour and steps correspond to 5σ (170 mJy beam^{-1} km s^{-1}) and 3σ, respectively.

(ii) g_2: the outflow cavity walls (∼20 arcsec, 60–80 K, 10^5–10^6 cm^{-3}) associated with the B1 ejection.

(iii) g_3: the older outflow cavity walls (extended, 20 K, $\simeq 10^5$ cm^{-3}) associated with the B2 ejection.

Lefloch et al. (2012) and Gómez-Ruiz et al. (2015) showed that each component is characterized by homogeneous excitation conditions independent of the velocity range (see Table 1). The intensity–velocity distribution of each component is well described by an exponential law $T_b(v) \propto \exp(v/v_0)$, where v_0 is almost independent of the molecular transition considered (v_0 = 12.5, 4.4, and 2.5 km s^{-1} for g_1, g_2, and g_3, respectively).

3 OBSERVATIONS

Observations of the IRAM Large Program ASAI were carried out during several runs between 2012 September and 2015 March. The nominal position observed are $\alpha_{J2000} = 20^{\rm h}\,39^{\rm m}\,10\overset{\rm s}{.}2$, $\delta_{J2000} = +68^\circ\,01'\,10''$ and $\alpha_{J2000} = 20^{\rm h}\,39^{\rm m}\,06\overset{\rm s}{.}3$, $\delta_{J2000} = +68^\circ\,02'\,15\overset{''}{.}8$ for L1157-B1 and L1157-mm, respectively.

Data were collected using the broad-band Eight MIxer Receiver (EMIR) receivers at 3 mm, 2 mm, 1.3 mm, whose interval frequencies are 72–116 GHz, 128–173 GHz, 200–272 GHz, respectively. Both the Fast Fourier Transform Spectrometers and the WILMA backends were connected to the EMIR receivers providing a spectral resolution of ∼200 kHz and 2 MHz, respectively. The FTS spectral resolution was degraded to a final velocity resolution of ≈1 km s^{-1}. In order to ensure a flat baseline across the spectral bandwidth observed, the observations were carried out in Wobbler Switching Mode, with a throw of 3 arcmin.

For the ASAI data, the reduction was performed using the GILDAS/CLASS software.[2] The calibration uncertainties are typically

[1] http://www.oan.es/asai/

[2] https://www.iram.fr/IRAMFR/GILDAS/

Table 1. Outflow shock components and their physical conditions in the L1157-B1 shock region, from CO and CS emission. The H_2 column densities were obtained from the CO column densities derived by Lefloch et al. (2012), adopting a CO/H_2 abundance ratio of 10^{-4} (see also Gómez-Ruiz et al. 2015).

	Vel. range (km s^{-1})	v_0 (km s^{-1})	T (K)	$n(H_2)$ (cm^{-3})	$N(H_2)$ (cm^{-2})	Size (arcsec)	Origin
g_1	−40; 0	12	210	≥1.0(6)	0.9(20)	7–10	Jet impact region
g_2	−20; 0	4	64	∼ 1.0(6)	0.9(21)	20	B1 outflow cavity walls
g_3	−8; 0	2	23	(0.5–2)(5)	1.0(21)	Extended	B2 outflow cavity walls

10, 15, and 20 per cent at 3 mm, 2 mm, and 1.3 mm, respectively. The line intensities are expressed in units of antenna temperature corrected for atmospheric attenuation and rearward losses (T_A^*). For subsequent analysis, fluxes are expressed in main beam temperature units (T_{mb}). The telescope and receiver parameters (beam efficiency, Beff; forward efficiency, Feff; Half Power beam Width, HPBW) were taken from the IRAM webpage.[3]

4 CYANOPOLYYNE EMISSION IN L1157-B1

The ASAI survey permitted the identification of several rotational transitions of HC_3N and HC_5N. The sensitivity of the survey permitted the detection of a few transitions of the ^{13}C isotopologues of HC_3N. We failed to detect larger cyanopolyynes as a search for HC_7N yielded only negative results. In this section, we describe the spectral signatures of HC_3N and HC_5N.

4.1 HC_3N

We detected all the HC_3N rotational transitions falling in the ASAI bands, from $J = 8$–7 ($E_{up} = 16$ K) up to $J = 29$–28 ($E_{up} = 189.9$ K). The spectra are displayed in Fig. 2. The line spectroscopic and observational properties are summarized in Table 2.

The bulk of the emission peaks at −1 km s^{-1}, with a linewidth (FWHM) ranging between 5 and 6 km s^{-1} (see Table 2). In the transitions with $J_{up} \leq 16$, emission is detected up to $v_{lsr} = -20$ km s^{-1}. The intensity–velocity distribution can be well fitted adopting a relation of the type $T \propto \exp(v/v_0)$ with $v_0 = +4$ km s^{-1}, independently of the rotational number of the transition (Fig. 3). This spectral signature has been observed in all the transitions, up to J = 25–24. In the lower J transitions, from $J = 8$–7 to $J = 19$–18, a second emission component with a lower velocity range, between 0 and −8 km s^{-1}, is detected. It can be fitted by a second exponential component with an exponent $v_0 = +2$ km s^{-1}, which, again, does not vary with J_{up} (Fig. 3).

This confirms that at least the high-J HC_3N line emission arises from component g_2, i.e. the outflow cavity associated with L1157-B1. In the top right panel of Fig. 3, we have superimposed the CS $J = 7$–6 spectrum (dashed red) on the HC_3N $J = 25$–24 line profile, applying a scaling factor so to match the peak intensity. We find an excellent match between both line profiles over the full emission range. This indicates that the high-J ($J \geq 25$) HC_3N line emission arises from component g_2. This point is further addressed in Section 5.

This profile decomposition is justified by the fact that the HC_3N line emission is optically thin, except at velocities close to that of the ambient cloud for the low-J transitions. We note, however, that the frequency of the transitions $J_{up} = 8$–12 is low enough that the telescope beam encompasses the shock region B0 (Fig. 1), which is associated with another ejection (Bachiller et al. 2001), so that the emission collected, and the line profiles, could be contaminated by this shock region. This point is addressed further below in Section 5.3.

The search for the HC_3N isotopologues yielded positive results in the band at 3 mm. We detected the transitions $H^{13}CCCN$ $J = 10$–9, 11–10, and 12–11; $HC^{13}CCN$ $J = 9$–8, 10–9, 11–10, 12–11; and $HCC^{13}CN$ $J = 9$–8, 10–9, 11–10, and 12–11, whose line profiles are displayed in Fig. 4. Intensity of all the transitions is weak, typically 5 mK (T_A^*), so that the line parameters determination suffers large uncertainties. Their properties are summarized in Table 2.

We searched for emission lines from the deuterated isotopologue of HC_3N, following the previous work by Codella et al. (2012) on the fossile deuteration in L1157-B1. We failed to detect any of the transitions falling in the 3mm ASAI band, down to a 3σ level of 4 mK (T_A^*).

4.2 HC_5N

Only transitions in the 3mm band, between 80 and 114 GHz, could be detected. All the transitions from $J = 30$–29 ($E_{up} = 59$ K) to $J = 43$–42 ($E_{up} = 121$ K) were detected down to the 3σ level (Table 2). Line intensities are rather weak, typically 5–10 mK, a factor of ∼20 less than HC_3N transitions of similar E_{up}. We show a montage of some HC_5N lines detected towards L1157-B1 in Fig. 5. The typical line width (FWHM) and the emission peak velocity are ≃4.5 km s^{-1} and −1 km s^{-1}, respectively, hence in good agreement with the parameters of the HC_3N lines. The analysis of the excitation conditions (see Section 5.3) leads us to conclude that the emission of HC_5N is dominated by g_2.

5 PHYSICAL CONDITIONS AND ABUNDANCES IN L1157-B1

The physical conditions and the column densities of HC_3N and HC_5N were obtained from the analysis of their Spectral Line Energy Distribution (SLED) via a Large Velocity Gradient (LVG) modelling and under the assumption of Local Thermodynamic Equilibrium (LTE), respectively. We discuss the two cases separately.

5.1 HC_3N

As discussed in the previous section, the HC_3N line emission can be decomposed in two components, g_2 and g_3, which probe the outflow cavity walls of B1 and B2, respectively. Fig. 6 shows the SLED of the two components. While the g_3 SLED peaks at $J \sim 11$, the g_2 SLED clearly shows two different peaks, at $J \leq 8$ and $J \sim 20$, suggesting the presence of a cold and a warm physical component.

Before modelling the SLED of each component, we first estimated the brightness temperature of the molecular lines. Our

[3] http://www.iram.es/IRAMES/mainWiki/Iram30mEfficiencies

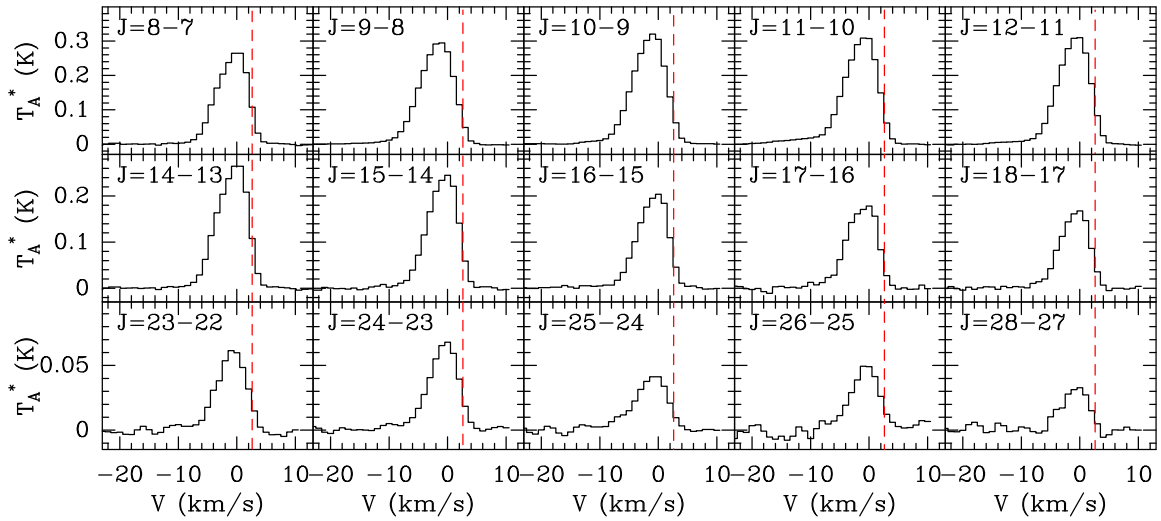

Figure 2. Montage of some HC_3N lines detected towards L1157-B1. The red line (dashed) draws the velocity of the cloud (v_{lsr} = +2.6 km s^{-1}).

previous studies of CO and CS showed that the component g_3 is extended enough that the brightness temperature of the lines can be approximated by the main-beam brightness temperature T_{mb}.

As the source size of component g_2 is not precisely known, we have chosen to perform the SLED modelling at a common angular resolution of 8.5 arcsec (the HPBW at the frequency of the J = 32–31 line, the highest detected transition of HC_3N in L1157-B1), for all the transitions. It means that the effective column density derived for the g_2 component scales as the effective filling factor in the 8.5 arcsec beam. To do so, we followed the methodology presented in Lefloch et al. (2012) and Gomez-Ruiz et al. (2015). The g_2 and g_3 velocity integrated fluxes used in our SLED analysis are reported in Table 3.

Taking into account the uncertainties in the spectral decomposition of component g_2 and g_3, we estimate the total uncertainties to be 15 per cent, 20 per cent, 25 per cent at 3 mm, 2 mm, and 1.3 mm, respectively.

To model the SLED emission, we used the LVG code by Ceccarelli et al. (2002) and used the collisional coefficients with para and ortho H_2 computed by Faure, Lique & Wiesenfeld (2016). For the H_2 ortho-to-para ratio we assumed the fixed value of 0.5, as suggested by previous observations. We ran a large grid of models with density between 10^4 cm^{-3} and 10^8 cm^{-3}, temperature between 15 K and 120 K, and the HC_3N column density between 2×10^{12} and 3×10^{14} cm^{-2}. We adopted $\Delta V = 5.5$ km s^{-1} and let the filling factor to be a free parameter in the case of the g_2 component. We then compared the LVG predictions and the observations and used the standard minimum reduced χ^2 criterion to constrain the four parameters: density, temperature, column density, and size (in g_2 only). The best-fitting LVG solutions are shown in Fig. 6.

The g_3 component SLED is well reproduced by an HC_3N column density $N(HC_3N) = 2.5 \times 10^{13}$ cm^{-2}, a temperature of 20 K, and a density $n(H_2) \simeq 2 \times 10^6$ cm^{-3}. Adopting an H_2 column density of 10^{21} cm^{-2} for g_3 (Table 1; Lefloch et al. 2012), we find a relative abundance $X(HC_3N) = 2.5 \times 10^{-8}$.

For the g_2 component, our modelling of the high-excitation lines (J_{up} = 14–29) shows that the best fit is obtained for $N(HC_3N) = 4 \times 10^{12}$ cm^{-2}, T_{kin} = 60 K, and $n(H_2) = 4 \times 10^6$ cm^{-3}, and a filling factor of 0.82, corresponding to a source size of 18 arcsec. This simple model fails, however, to reproduce the low excitation range J_{up} = 8–12 of the SLED (see Fig. 6). A second gas component with a lower density $n(H_2) = 6 \times 10^4$ cm^{-3} and lower temperature T = 20 K is needed to account for the total observed flux. We estimate for this component a column density $N(HC_3N) = 2 \times 10^{13}$ cm^{-2}, and a size of 10 arcsec. These physical conditions differ from those of g_2 and g_3 (see also Section 2). As pointed out in Section 4.1, in the frequency range corresponding to the J = 8–12 transitions, the beam size is large enough (≥23 arcsec) that it encompasses the shock region B0, which thereby contributes to the collected emission. Conversely, at frequencies higher than that of the J = 15–14 line, the beam size (HPBW) is about ≤18 arcsec, and the telescope beam misses the B0 emission. This is probably the cause of the observed excess in the low J emission lines. We note that the density of the high-velocity bullets reported by Benedettini et al. (2013) is lower by a factor of a few in the B0 region, as compared to the B1 region; it is in agreement with the values obtained in the present analysis. Also, Lefloch et al. (2012) showed that the g_2 spectral signature was actually detected along the entire walls of the B1 cavity, between the protostar L1157-mm and the apex where bright molecular emission is detected. Proceeding as above for component g_3, we obtain an abundance of 4×10^{-9} cm^{-2} for HC_3N in component g_2. The physical properties of the HC_3N isotopologues towards L1157-B1 (and L1157-mm) are summarized in Table 4. The cyanopolyyne abundances determined towards L1157-B1 (and L1157-mm) are summarized in Table 5.

To summarize, the HC_3N emission arises from two physical components, g_3 and g_2, respectively, with an abundance relative to H_2 of 2.5×10^{-8} and 4×10^{-9}, respectively. These results are consistent with the previous work by Bachiller & Pérez-Gutíerrez (1997). These authors estimated an abundance relative to H_2 of 1.0×10^{-8}, assuming one single gas component, from the detection of the three HC_3N J = 10–9, 15–14, 14–23 lines in the shock. Interestingly, the abundance of HC_3N towards g_2 appears lower than towards g_3, as low as a factor of 6.

5.2 The rare isotopologues of HC_3N

5.2.1 $H^{13}CCCN$, $HC^{13}CCN$, and $HCC^{13}CN$

Only the transitions from $H^{13}CCCN$, $HC^{13}CCN$, and $HCC^{13}CN$ with E_{up} between 19 and 34 K were detected. The low number (3–4) of detected transitions for each isotopologue prevents us from

Table 2. L1157-B1. Spectroscopic and observational parameters of the lines from HC_3N, its isotopologues, and HC_5N identified towards the protostellar shock L1157-B1. We give in bracket the statistical uncertainties on the observational parameters, as derived from a gauss fit to the profiles.

Transition $J \rightarrow J-1$	Frequency MHz	E_u K	A_{ul} s^{-1}	HPBW arcsec	η_{mb}	$\int T_{mb} dv$ mK km s^{-1}	FWHM km s^{-1}	V_{lsr} km s^{-1}
HC_3N								
8–7	72783.822	15.7	2.94(−5)	33.8	0.86	2044(3)	5.9(0.1)	−0.7(0.1)
9–8	81881.468	19.7	4.21(−5)	30.0	0.85	2556(4)	6.2(0.2)	−1.7(0.1)
10–9	90979.023	24.0	5.81(−5)	27.0	0.84	2674(4)	6.1(0.2)	−1.4(0.1)
11–10	100076.392	28.8	7.77(−5)	24.6	0.84	2729(7)	6.2(0.1)	−1.3(0.1)
12–11	109173.634	34.1	1.01(−4)	22.5	0.83	2560(7)	5.9(0.1)	−1.0(0.1)
14–13	127367.666	45.9	1.62(−4)	19.3	0.81	1790(8)	5.8(0.1)	−0.9(0.1)
15–14	136464.411	52.4	1.99(−4)	18.0	0.81	1951(9)	5.8(0.1)	−0.8(0.1)
16–15	145560.960	59.4	2.42(−4)	16.9	0.79	1659(9)	5.8(0.1)	−0.9(0.1)
17–16	154657.284	66.8	2.91(−4)	15.9	0.77	1516(19)	5.9(0.1)	−1.1(0.1)
18–17	163753.389	74.7	3.46(−4)	15.0	0.77	1370(12)	5.6(0.1)	−0.8(0.1)
19–18	172849.301	83.0	4.08(−4)	14.2	0.75	1248(92)	5.9(0.3)	−1.1(0.2)
23–22	209230.234	120.5	7.26(−4)	11.8	0.67	543(9)	5.7(0.2)	−0.8(0.1)
24–23	218324.723	131.0	8.26(−4)	11.3	0.65	611(10)	5.3(0.2)	−0.6(0.1)
25–24	227418.905	141.9	9.35(−4)	10.8	0.64	430(8)	6.1(0.3)	−1.1(0.1)
26–25	236512.789	153.2	1.05(−3)	10.4	0.63	451(14)	5.3(0.4)	−0.6(0.1)
27–26	245606.320	165.0	1.18(−3)	10.0	0.62	273(10)	7.1(0.4)	−0.9(0.2)
28–27	254699.500	177.3	1.32(−3)	9.7	0.60	289(12)	4.9(0.4)	−0.8(0.2)
29–28	263792.308	189.9	1.46(−3)	9.3	0.60	187(16)	5.0(0.8)	−0.5(0.3)
$H^{13}CCCN$								
10–9	88166.832	23.3	5.29(−5)	27.9	0.85	40.7(4.5)	7.1(1.4)	−1.8(0.5)
11–10	96983.001	27.9	7.07(−5)	25.4	0.85	76.0(4.8)	7.2(1.0)	−0.8(0.4)
12–11	105799.113	33.0	9.21(−5)	23.3	0.84	48.1(3.9)	5.2(0.8)	−2.3(0.3)
$HC^{13}CCN$								
9–8	81534.111	19.6	4.16(−5)	30.2	0.86	55.8(2.7)	6.1(0.9)	−2.7(0.3)
10–9	90593.059	23.9	5.74(−5)	27.2	0.85	43.1(3.7)	6.5(1.5)	−3.8(0.5)
11–10	99651.849	28.7	7.67(−5)	24.7	0.84	43.6(5.2)	5.0(1.7)	−0.4(0.7)
12–11	108710.532	33.9	1.00(−4)	22.6	0.83	31.3(5.0)	6.1(2.7)	−0.7(0.9)
$HCC^{13}CN$								
9–8	81541.981	19.6	4.16(−5)	30.2	0.86	25.7(3.1)	4.5(1.4)	−0.7(0.6)
10–9	90601.777	23.9	5.74(−5)	27.2	0.85	38.1(4.2)	4.8(1.6)	−1.8(0.6)
11–10	99661.467	28.7	7.67(−5)	24.7	0.84	33.3(5.3)	4.5(2.0)	−1.1(0.8)
12–11	108720.999	33.9	1.00(−4)	22.6	0.83	35.5(3.4)	4.0(0.7)	−0.4(0.3)
HC_5N								
30–29	79876.710	59.4	5.47(−5)	30.8	0.86	39.1(3.4)	3.5(0.8)	−1.5(0.3)
31–30	82539.039	63.4	6.04(−5)	29.8	0.85	22.5(1.7)	3.7(0.8)	−1.7(0.3)
32–31	85201.346	67.5	6.64(−5)	28.9	0.85	34.1(1.7)	5.0(0.8)	−1.9(0.3)
33–32	87863.630	71.7	7.29(−5)	28.0	0.85	47.1(1.5)	7.4(1.0)	−1.8(0.4)
34–33	90525.889	76.0	7.98(−5)	27.2	0.85	37.1(1.7)	6.3(1.2)	−1.5(0.5)
35–34	93188.123	80.5	8.71(−5)	26.4	0.85	30.8(2.6)	5.4(2.3)	−0.6(0.7)
36–35	95850.335	85.1	9.48(−5)	25.7	0.85	36.0(2.4)	5.7(1.4)	−0.4(0.6)
37–36	98512.524	89.8	1.03(−4)	25.0	0.84	27.9(1.2)	3.5(0.8)	1.8(0.6)
38–37	101174.677	94.7	1.12(−4)	24.3	0.84	38.2(2.0)	7.6(2.1)	−2.2(0.9)
39–38	103836.817	99.7	1.21(−4)	23.7	0.84	31.1(2.0)	6.0(1.6)	−2.7(0.6)
40–39	106498.910	104.8	1.30(−4)	23.1	0.84	39.2(2.2)	5.0(1.0)	0.2(0.4)
41–40	109160.973	110.0	1.40(−4)	22.5	0.83	28.2(2.2)	5.0(2.1)	−2.3(0.8)
42–41	111823.024	115.4	1.51(-4)	22.0	0.83	45.0(3.4)	4.4(1.0)	0.2(0.4)
43–42	114485.033	120.9	1.62(-4)	21.5	0.83	23.0(3.9)	2.9(1.1)	−0.8(0.5)

carrying out a detailed analysis of the emission, similar to the approach adopted for HC_3N. In addition, our analysis of the HC_3N emission shows that in this range of E_{up}, the emission is dominated by g_3 and most probably contaminated by emission from the shock region B0, so that even a rotational diagram analysis would be somewhat not significant.

We have just simply assumed that the emission of the ^{13}C-bearing isotopes and of the main isotope in the J = 9–8 to J = 12–11 lines originates from the same gas so that the corresponding line flux ratios provide a reliable measurement of the molecular abundance ratios if the main isotopologue is optically thin. The mean flux ratios are 52 ± 15, 63 ± 20, and 81 ± 10, for $HC^{13}CCN$, $HC^{13}CCN$, and $HCC^{13}CN$, respectively. These results do not show any significant difference between the three ^{13}C-bearing isotopes that could indicate a differential ^{13}C fractionation between the three HC_3N isotopologues. These molecular abundance ratios are also

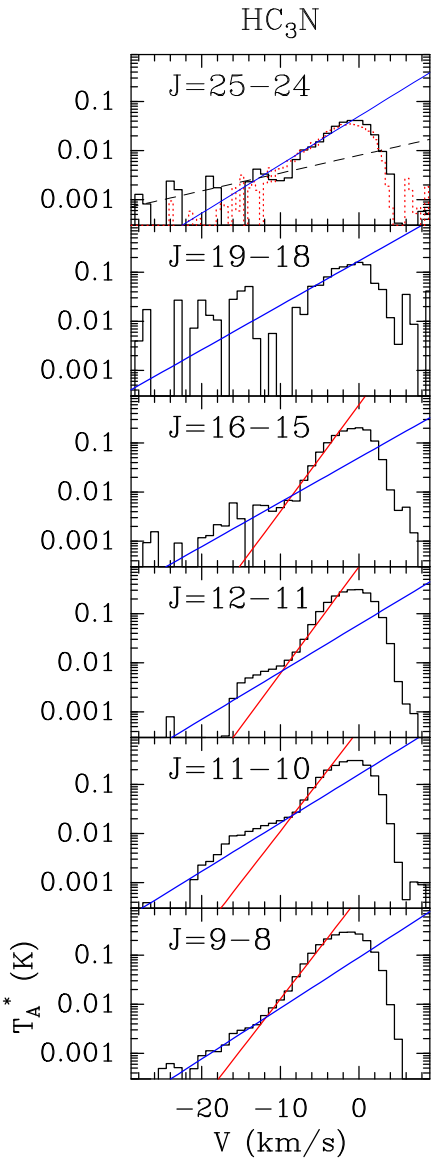

Figure 3. Montage of some HC_3N spectra detected towards L1157-B1. We have superimposed the fit obtained by a linear combination of two exponential functions $g_2 \propto \exp(-v/4.0)$ (blue) and $g_3 \propto \exp(-v/2.0)$ (red). In the top panel (J = 25–24), a fit of the g_1 component ($\propto \exp(-v/12)$) is superimposed in black and the CS J = 7–6 line (a proxy for the g_2 component) is superimposed in dotted red.

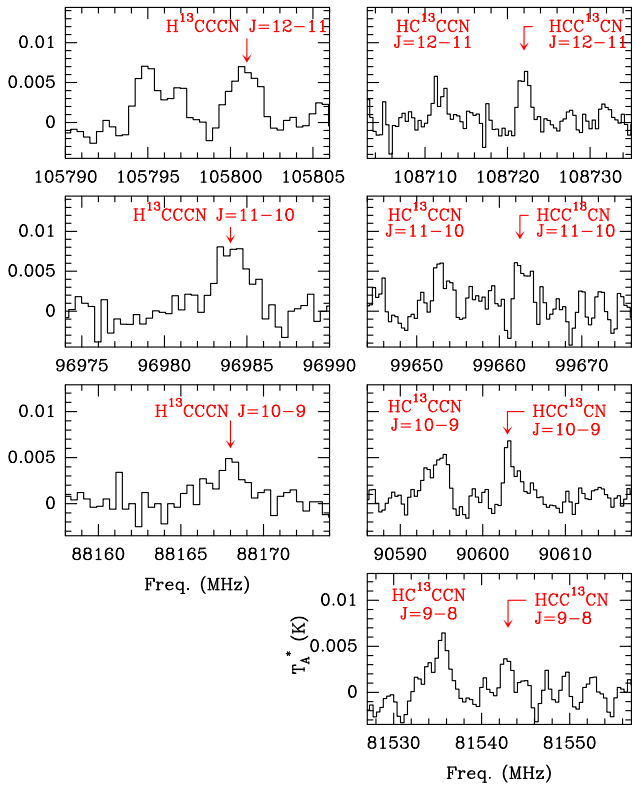

Figure 4. Montage of the detected transitions from the rare isotopologues $H^{13}CCCN$, $HC^{13}CCN$, and $HCC^{13}CN$.

consistent with a standard value for the elemental abundance ratio $^{12}C/^{13}C$ of 70, which is consistent with the ^{12}C isotopologue being optically thin.

5.2.2 DC_3N

None of the DC_3N lines falling in the 3mm band were detected, down to an rms of 1.4 mK. We obtained an upper limit on the column density of DC_3N in the LTE approximation. We adopted the value T_{rot} = 25 K, obtained for HC_3N in the same range of E_{up} (18–69 K). Since the HC_3N emission is dominated by component g_3 in this range of E_{up}, we assumed DC_3N to arise from the same region, and to be extended. We obtain as upper limit $N(DC_3N) = 5 \times 10^{10}$ cm^{-2}, from which we derive an upper limit on the

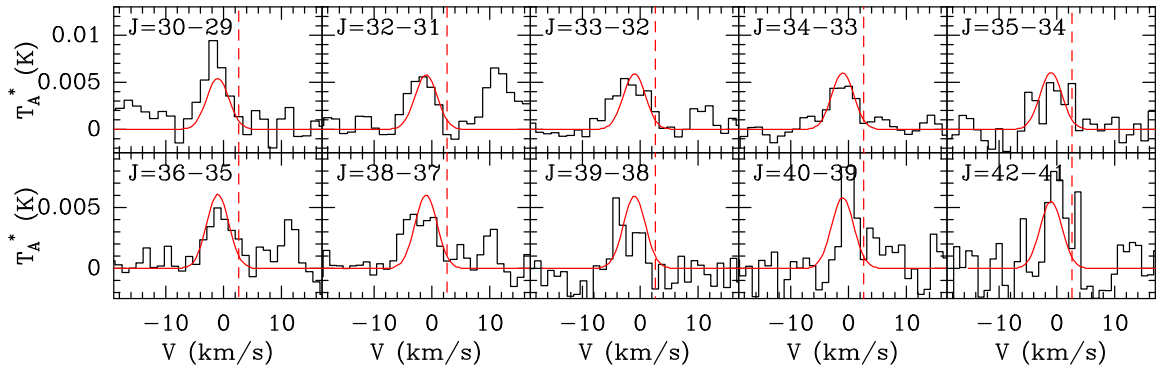

Figure 5. Montage of some HC_5N transitions detected towards L1157-B1. The best fit obtained from a simple rotational diagram analysis is shown in red, adopting a linewidth Δv = 5 km s^{-1}. The ambient cloud velocity (v_{lsr} = +2.6 km s^{-1}) is marked by the dash–dotted line.

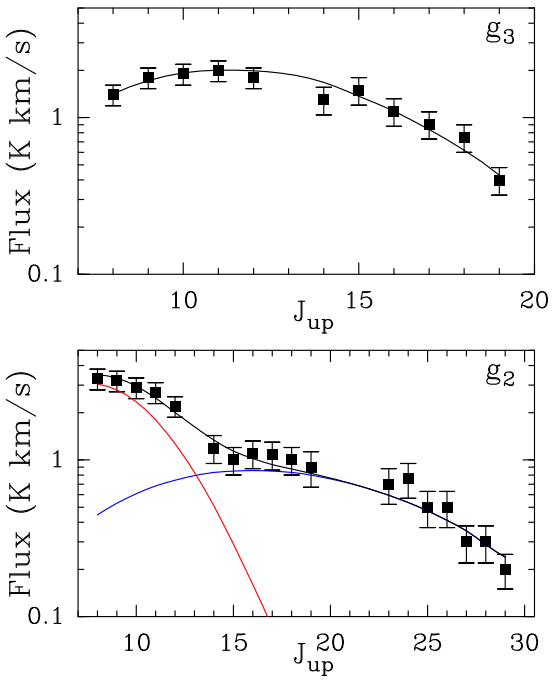

Figure 6. Modelling of the HC_3N SLED with a simple LVG slab model. The black squares represent the measured velocity-integrated fluxes for components g_2 (bottom) and g_3 (top). They are expressed in units of main-beam brightness temperatures (T_{mb}). Top panel: the solid curve shows the LVG predictions for component g_3 assuming one single gas component with a column density $N(HC_3N) = 2.5 \times 10^{13}$ cm^{-2}, a temperature of 20 K, and a density $n(H_2)$ 2×10^6 cm^{-3}. Bottom panel: the solid curves show the LVG predictions for component g_2, obtained assuming two components at 20 K (red), with density $n(H_2) = 6 \times 10^4$ cm^{-3}, $N(HC_3N) = 2 \times 10^{13}$ cm^{-2} and at 60 K (blue), with density $n(H_2) = 4 \times 10^6$ cm^{-3}, $N(HC_3N) = 4 \times 10^{12}$ cm^{-2}, respectively.

Table 3. HC_3N velocity-integrated intensities of the components g_2 and g_3 used in the radiative transfer calculations. Fluxes are expressed in units of brightness temperature in a beam of 8.5 arcsec for g_2 and in main-beam brightness temperature for g_3, respectively.

Transition	Frequency (MHz)	ff (g_2)	Flux (g_2) K km s^{-1}	Flux (g_3) K km s^{-1}
8–7	72 783.822	0.184	3.34	1.43
9–8	81 881.468	0.227	3.23	1.83
10–9	90 979.023	0.268	2.91	1.89
11–10	100 076.392	0.310	2.52	1.95
12–11	109 173.634	0.354	2.24	1.77
14–13	127 367.666	0.437	1.02	1.34
15–14	136 464.411	0.482	0.97	1.49
16–15	145 560.960	0.522	1.13	1.07
17–16	154 657.284	0.563	1.29	0.91
18–17	163 753.389	0.603	1.01	0.76
19–18	172 849.301	0.642	0.90	0.40
23–22	209 230.234	0.775	0.70	0.0
24–23	218 324.723	0.807	0.76	0.0
25–24	227 418.905	0.839	0.51	0.0
26–25	236 512.789	0.866	0.52	0.0
27–26	245 606.320	0.892	0.30	0.0
28–27	254 699.500	0.914	0.32	0.0
29–28	263 792.308	0.942	0.20	0.0

Table 4. Properties of the HC3N isotopologues towards L1157-B1 and the cold envelope of L1157-mm. Cases where no estimate could be obtained are indicated by '-'.

Species		L1157-B1		L1157-mm	
		g_3	g_2		
HC_3N	Size (arcsec)	Extended	18	20	5
	N(cm^{-2})	2.5(13)	4.0(12)	5.3(12)	7.2(12)
	T(K)	20	60	10	30
	$n(H_2)$	2(6)	4(6)	–	–
DC_3N	Size (arcsec)	Extended	–	20	–
	N(cm^{-2})	<5(10)	–	(3.4–5.2)(11)	–
	T(K)	25	–	11–23	–

Table 5. Cyanopolyyne abundances determined towards L1157-B1 and the cold envelope of L1157-mm. Cases where no estimate could be obtained are indicated by '-'.

Species	L1157-B1		L1157-mm
	g_3	g_2	
HC_3N	2.5(−8)	4.0(−9)	0.9(−9)
HC_5N	–	1.2(−9)	–

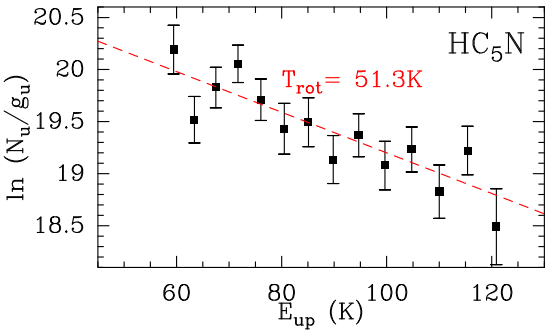

Figure 7. Rotational diagram of HC_5N. The emission was corrected for the coupling between the source and the telescope beam assuming a typical size of 18 arcsec.

abundance [DC_3N] = 5 × 10^{-11} and the deuterium fractionation ratio D/H = 0.002.

5.3 HC_5N

The physical conditions of HC_5N were obtained from a simple rotational diagram analysis, as shown in Fig. 7. The spatial distribution of HC_5N is not constrained and we considered two cases: (a) HC_5N arises from g_3, and the emission is so extended that the line brightness is well approximated by the line main-beam temperature; (b) HC_5N arises from g_2, with a typical size of 18 arcsec. Case (a) can be ruled out as the best-fitting solution provides a rotational temperature $T_{rot} = 87 \pm 26$ K, which is not consistent with the kinetic temperature of that component (20–25 K). For Case (b), the emission of the detected transitions can be reasonably well described by one gas component with $T_{rot} = (51.3 \pm 8.9)$ K and column density $N(HC_5N) = (1.2 \pm 0.4) \times 10^{12}$ cm^{-2}. This is consistent with the gas kinetic temperature of component g_2 (≈60 K). Based on our analysis of the excitation conditions we conclude that the emission of HC_5N is dominated by g_2 and the abundance [HC_5N] is ≈1.2×10^{-9}. The best-fitting solution to the line profiles is shown in Fig. 5. We note that the HC_3N column density is ≃4.0×10^{12} cm^{-2} in the same

range of excitation conditions, hence the relative abundance ratio $HC_3N/HC_5N \simeq 3.3$.

5.4 HC_7N

The non-detection of HC_7N could be due to a lower abundance (like in TMC1) and/or to less favourable excitation conditions than for the smaller cyanopolyynes. The lowest frequency transition in the ASAI band is $J = 64$–63, 72187.9088 MHz has an $E_{up} = 112.6$ K. Between 80 and 114 GHz, the frequency interval in which HC_5N lines are detected, HC_7N lines have E_{up} between 140 and 250 K. These values are higher than the highest E_{up} transition of HC_5N detected. We note that a factor of 2–3 less in abundance would suffice to hamper any detection. In practice, we could only place an upper limit on the HC_7N abundance of $\approx 5 \times 10^{-8}$. Observations at lower frequency with the Green Bank Telescope or the VLA would help in confirming or not the presence of this molecule in the shock.

6 THE PROTOSTAR L1157-MM

In order to better understand the impact of the B1 shock on the ambient gas chemistry, we conducted a similar analysis towards the envelope of the protostar L1157-mm, which drives the outflow responsible for the shock L1157-B1. We searched for and detected the emission of HC_3N transitions between $J = 8$–7 and $J = 28$–27, as well as of deuterated isotopologue DC_3N between $J = 9$–8 and $J = 18$–17 (Figs A1–A3). We note that the latter molecule was not detected in the shock. We failed to detect the emission from the rare ^{13}C isotopologues. Four transitions of HC_5N were detected ($J = 31$–30, 32–31, 34–33, and 40–39). Unfortunately, the number of detected HC_5N lines is too low and the flux uncertainties are too large to allow a detailed modelling of the emission. They will no longer be considered in what follows.

The emission was analysed under the LTE hypothesis and following the same methodology as for the shock region. In order to ease the reading, we present in this section only our results. The data and the radiative transfer modelling are presented in the Appendix.

Linewidths are much narrower towards L1157-mm, with $\Delta v \simeq 1.5$–2.5 km s^{-1}. Overall, we detected less transitions towards L1157-mm (see Table A1); in particular, we missed the emission from the high-J levels detected towards the shock (see Figs A1–A3).

As can be seen in Fig. A2, the HC_3N emission can be described by the sum of two physical components: first, a low-excitation component with $T_{rot} = (10.0 \pm 0.3)$ K and $N(HC_3N) = (5.3 \pm 0.6) \times 10^{12}$ cm^{-2}, adopting a size of 20 arcsec for the envelope, based on submm continuum observations of the region by Chini et al. (2001), and second, a higher-excitation component with $T_{rot} = (31.3 \pm 1.2)$ K and $N(HC_3N) = (7.2 \pm 1.0) \times 10^{12}$ cm^{-2}, adopting a size of 5 arcsec. We estimated the total H_2 column density of the envelope from LTE modelling of flux of the ^{13}CO $J =$ 1–0 line, adopting an excitation temperature of 10 K and a source size of 20 arcsec, and a standard abundance ratio $[^{13}CO]/[H_2] = 1.6 \times 10^{-6}$. From this simple analysis, we derive a relative abundance $X(HC_3N) = 9 \times 10^{-10}$ for the cold protostellar envelope. The uncertainty on the size of the warm gas component and the H_2 column density makes it difficult to estimate molecular abundances in that region. Interferometer observations are required to better estimate these abundances.

The DC_3N emission arises from transitions with E_{up} in the range 18–70 K (Table A1). Analysis of the DC_3N lines yields $T_{rot} = (22.9 \pm 1.9)$ K and $N(DC_3N) = (3.4 \pm 0.6) \times 10^{11}$ cm^{-2}, adopting a size of 20 arcsec (Fig. A4). In the $E_{up} < 40$ K range, the emission of the main HC_3N isotopologue is dominated by the low-excitation component with $T_{rot} = 10$ K (Fig. A2). Under the reasonable assumption that DC_3N is dominated by the same gas component, we obtain a relatively high value of the deuterium fractionation ratio D/H = 0.06. In addition, considering only the transitions of lowest E_{up} between 18 and 27 K, a fit to the DC_3N data yields $T_{rot} = (10.9 \pm 1.7)$ K, in even better agreement with the results for the low-excitation HC_3N component, and $N(DC_3N) = (5.2 \pm 1.8) \times 10^{11}$ cm^{-2}. This supports the reasonable assumption that DC_3N and HC_3N trace the same gas region and the corresponding D/H ratio is 0.10.

7 DISCUSSION

7.1 Shock initial conditions

We can obtain a qualitative picture of the shock impact on cyanopolyyne chemistry from the assumption that the chemical and excitation conditions in the pre-shock molecular gas are rather similar to those in the envelope of L1157-mm. In the outer regions of the latter, we estimate a typical abundance of $\sim 10^{-9}$, which implies that the molecular abundance of HC_3N has been increased by a factor of about 30 through the passage of the shock.

The deuterium fractionation of HC_3N is rather large in the protostellar envelope (D/H = 0.06), whereas DC_3N is not detected in the shocked gas of L1157-B1, with an upper limit of 0.002 on the D/H ratio in L1157-B1. We note that if the shock production of HC_3N is not accompanied by any DC_3N gas phase enrichment, then the deuterium fractionation ratio is simply 30 times less, and D/H becomes 0.002, the upper limit obtained with ASAI. Hence, DC_3N was probably not affected by the same abundance enhancement as its main isotopologue. This implies a low deuterium fractionation for HC_3N produced in the shock, either from grain sputtering or from gas phase reactions. In both cases, HC_3N must have formed in warm (hot) gas. This is also consistent with the absence of ^{13}C fractionation of HC_3N.

7.2 The HC_3N/HC_5N ratio

The high sensitivity of the ASAI data has allowed us to detect the emission of HC_5N, for the first time in a shock. Jaber Al-Edhari et al. (2017) have studied the HC_3N and HC_5N abundance distribution in different Galactic environments. The abundance values we found in component g_2 for HC_3N and HC_5N, 4.0×10^{-9} and 1.2×10^{-9}, respectively, are among the highest values reported towards Galactic objects. They are typically higher than those found towards hot corino and WCCC sources by one to two orders of magnitude. In particular, we found that the HC_5N abundance in L1157-B1 is higher than in the hot corino of IRAS16293−2422 by a factor of about 30.

In their study, Jaber Al-Edhari et al. (2017) showed that a low ($\approx$1) relative abundance ratio HC_3N/HC_5N is typical of 'cold', low-luminosity objects like early protostars (first hydrostatic core candidates) and WCCC sources (see e.g. Sakai et al. 2008). Analysis of the molecular content of the L1157-mm envelope recently led Lefloch et al. (2017b) to classify it as a WCCC protostar. Then, a low abundance ratio $X(HC_3N)/X(HC_5N)$ is to be expected in the L1157-mm envelope. The rather low abundance ratio $X(HC_3N)/X(HC_5N)$ measured in the shock component g_2 ($\approx$3.3) suggests that the abundance of HC_5N has increased by a factor similar to that of HC_3N in the shock. In general, based on the models shown in Fontani et al. (2017), a low HC_3N/HC_5N abundance ratio points towards an

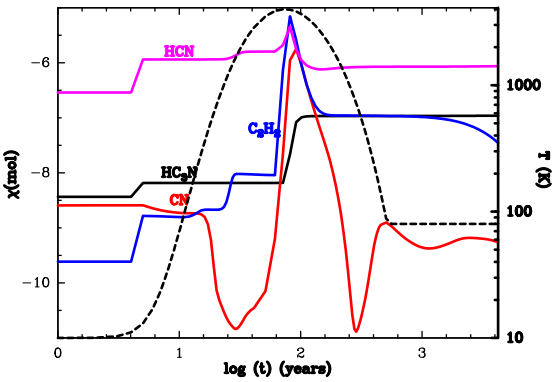

Figure 8. Modelling of HC_3N (black) and its potential precursors HCN (magenta), C_2H_2 (blue), and CN (red), in L1157-B1. The temperature profile across the shock is displayed with the black dashed line.

early time chemistry where the injected new carbon (as CH_4, CO or another species) is rapidly used for carbon chain formation and only later (re-)forms CO. It would be interesting to probe lower-excitation transitions of HC_5N to determine its abundance in the outer envelope of L1157-mm and the low-excitation component g_3 of the shock.

7.3 Shock modelling

In order to determine whether HC_3N arises in the shocked gas of the L1157-B1 cavity, we consider the best-fitting chemical and parametric shock model from previous works by our team (Viti et al. 2011; Holdship et al. 2016; Lefloch et al. 2016), namely one where the pre-shock density is 10^5 cm^{-3} and the shock velocity is 40 km s^{-1}. In Fig. 8, we plot the fractional abundance of HC_3N, and other selected species, as a function of time. We find that the abundance of HC_3N increases at two different times: the first increase is due to mantle sputtering due to the passage of the shock. The second increase is, in fact, due to the reaction of CN with C_2H_2: CN + $C_2H_2 \rightarrow HC_3N + H$. This channel has an increased efficiency when the temperature is much higher than 300 K due to the dependence of this reaction to temperature (Woon & Herbst 1997) but, most importantly, due to the enhanced C_2H_2 and CN abundances when the temperature is at its maximum (∼4000 K). Indeed, C_2H_2 and CN form via neutral-neutral reactions whose efficiency increases with temperature. In summary, the HC_3N abundance increases strongly as a consequence of the passage of the shock; this is consistent with the fact that observationally HC_3N appears to be enhanced (by a factor of 30) towards the shocked position of L1157-B1. Our modelling shows that the HC_3N abundance enrichment is dominated by the high-temperature gas phase reactions rather than sputtering of frozen HC_3N on to dust grains. This is consistent with the absence of differential fractionation between the three rare ^{13}C isotopologues and the low deuterium enrichment when compared with the envelope of L1157-mm.

8 CONCLUSIONS

As part of ASAI, we have carried out a systematic search for cyanopolyynes $HC_{2n+1}N$ towards the protostellar outflow shock region L1157-B1 and the protostar L1157-mm, at the origin of the outflow phenomenon. Towards L1157-B1, we confirm the detection of HC_3N lines $J = 8$–7 to $J = 29$–28 and we report the detection of transitions from its ^{13}C isotopologues $J = 9$–8 to $J = 12$–11. We have detected the HC_5N lines $J = 30$–29 to $J = 43$–42 for the first time in a shock. Towards L1157-mm, we detected the HC_3N lines $J = 8$–7 to $J = 28$–27 and the deuterated isotopologue DC_3N lines $J = 9$–8 to $J = 18$–17. We summarize our main results as follows.

(i) The abundance of HC_3N has been increased by a factor of about 30 in the passage of the shock.

(ii) The upper limit we can place on the deuterium fraction ratio D/H in the shock (0.002) shows that the abundance enhancement of HC_3N was not accompanied by a significant abundance enhancement of DC_3N, which is consistent with a warm gas phase formation scenario. This is also supported by the observed lack of ^{13}C fractionation of HC_3N.

(iii) The rather low abundance ratio $X(HC_3N)/X(HC_5N)$ measured in L1157-B1 suggests that HC_5N was also efficiently formed in the shock.

(iv) A simple modelling based on the shock code of Viti et al. (2011) and the chemical code UCL_CHEM, adopting the best-fitting solution determined from previous work on L1157-B1 by our team, accounts for the above observational results. The HC_3N abundance increases in a first step as a result of grain mantle sputtering and, in a second step, as a result of the very efficient gas phase reaction of CN with C_2H_2.

ACKNOWLEDGEMENTS

Based on observations carried out as part of the Large Program ASAI (project number 012-12) with the IRAM 30-m telescope. IRAM is supported by INSU/CNRS (France), MPG (Germany) and IGN (Spain). This work was supported by the CNRS program "Physique et Chimie du Milieu Interstellaire" (PCMI) and by a grant from LabeX Osug@2020 (Investissements d'avenir - ANR10LABX56). E. M. acknowledges support from the Brazilian agency FAPESP (grant 2014/22095-6 and 2015/22254-0). I.J.-S. acknowledges the financial support received from the STFC through an Ernest Rutherford Fellowship (proposal number ST/L004801/1).

REFERENCES

Bachiller R., Pérez Gutiérrez M., 1997, ApJ, 487, L93
Bachiller R., Pérez Gutiérrez M., Kumar M. S. N., Tafalla M., 2001, A&A, 372, 899
Bell M. B., Feldman P. A., Travers M. J., McCarthy M. C., Gottlieb C. A., Thaddeus P., 1997, ApJ, 483, L61
Benedettini M. et al., 2012, A&A, 539, L3
Benedettini M. et al., 2013, MNRAS, 436, 179
Busquet G. et al., 2014, A&A, 561, 120
Ceccarelli C. et al., 2002, A&A, 383, 603
Cernicharo J., Guélin M., 1996, A&A, 309, L27
Chini R., Ward-Thompson D., Kirk J. M., Nielbock M., Reipurth B., Sievers A., 2001, A&A, 369, 155
Clarke D. W., Ferris J. P., 1995, Icarus, 155, 119
Codella C. et al., 2010, A&A, 518, L112
Codella C. et al., 2012, ApJ, 757, L9
Codella C., Fontani F., Ceccarelli C., Podio L., Viti S., Bachiller R., Benedettini M., Lefloch B., 2015, MNRAS, 449, L11
Codella C. et al., 2017, A&A, 605, L3
Cordiner M. A., Charnley S. B., Wirström E. S., Smith R. G., 2012, ApJ, 744, 131
Couepaud A., Kolos R., Couturier-Tamburelli I., Aycard J. P., Pietri N., 2006, J. Phys. Chem. A, 110, 2371
Crovisier J. et al., 2004, A&A, 418, 1141
Faure A., Lique F., Wiesenfeld L., 2016, MNRAS, 460, 2103
Fontani F. et al., 2017, A&A, 605, 57

Friesen R. K., Medeiros L., Schnee S., Bourke T. L., Francesco J. Di, Gutermuth R., Myers P. C., 2013, MNRAS, 436, 1513
Gómez-Ruiz A. I. et al., 2015, MNRAS, 446, 3346
Gueth F., Guilloteau S., Bachiller R., 1996, A&A, 307, 891
Gueth F., Guilloteau S., Bachiller R., 1998, A&A, 333, 287
Holdship J. et al., 2016, MNRAS, 463, 802
Jaber Al-Edhari A. et al., 2017, A&A, 597, 40
Lefloch B. et al., 2010, A&A, 518, L113
Lefloch B. et al., 2012, ApJ, 757, L25
Lefloch B. et al., 2016, MNRAS, 462, 3937
Lefloch B. et al., 2017a, submitted
Lefloch B., Ceccarelli C., Codella C., Favre C., Podio L., Vastel C., Viti S., Bachiller R., 2017b, MNRAS, 469, L73
Looney L., Tobin J., Kwon W., 2007, ApJ, 670, L131
Mendoza E., Lefloch B., López-Sepulcre A., Ceccarelli C., Codella C., Boechat-Roberty H. M., Bachiller R., 2014, MNRAS, 445, 151
Podio L., Lefloch B., Ceccarelli C., Codella C., Bachiller R., 2014, A&A, 565, A64
Podio L. et al., 2016, A&A, 593, L4
Podio L. et al., 2017, MNRAS, 470, L16
Sakai N., Sakai T., Hitora T., Yamamoto S., 2008, ApJ, 672, 371
Tafalla M., Bachiller R., 1995, ApJ, 443, L37
Tafalla M., Bachiller R., Lefloch B., Rodríguez-Fernández N., Codella C., López-Sepulcre A., Podio L., 2015, A&A, 573, L2
Takano S. et al., 1998, A&A, 329, 1156
Takano S. et al., 2014, PASJ, 66, 75
Viti S., Jiménez-Serra I., Yates J. A., Codella C., Vasta M., Caselli P., Lefloch B., Ceccarelli C., 2011, ApJ, 740, L3
Woon D. E., Herbst E., 1997, ApJ, 477, 204
Yamaguchi T. et al., 2012, PASJ, 64, 105

APPENDIX: CYANOPOLYYNE EMISSION IN L1157-MM

Table A1. Spectroscopic and observational parameters of the lines from HC_3N and its isotopologues identified towards the protostar L1157-mm. We give in bracket the statistical uncertainties on the observational parameters, as derived from a gauss fit to the profiles.

Transition $J \rightarrow J-1$	Frequency MHz	E_u K	A_{ul} s^{-1}	HPBW arcsec	η_{mb}	$\int T_{mb} dv$ mK km s^{-1}	FWHM km s^{-1}	V_{lsr} km s^{-1}
HC_3N								
8–7	72 783.822	15.7	2.94(−5)	33.8	0.86	338(4)	2.3(0.8)	3.0(0.1)
9–8	81 881.468	19.7	4.21(−5)	30.0	0.85	305(4)	1.7(0.7)	2.3(0.1)
10–9	90 979.023	24.0	5.81(−5)	27.0	0.84	330(4)	1.7(0.6)	2.9(0.1)
11–10	100 076.392	28.8	7.77(−5)	24.6	0.84	264(7)	1.5(0.6)	2.8(0.1)
12–11	109 173.634	34.1	1.01(−4)	22.5	0.83	267(7)	1.4(0.5)	2.4(0.1)
14–13	127 367.666	45.9	1.62(−4)	19.3	0.81	189(8)	1.3(0.5)	2.5(0.1)
15–14	136 464.411	52.4	1.99(−4)	18.0	0.81	178(9)	1.4(0.4)	2.6(0.1)
16–15	145 560.960	59.4	2.42(−4)	16.9	0.79	141(9)	1.1(0.4)	2.5(0.1)
17–16	154 657.284	66.8	2.91(−4)	15.9	0.77	113(19)	1.1(0.4)	2.7(0.1)
18–17	163 753.389	74.7	3.46(−4)	15.0	0.77	99(12)	1.4(0.4)	2.5(0.1)
23–22	209 230.234	120.5	7.26(−4)	11.8	0.67	72(9)	1.5(0.2)	2.5(0.1)
24–23	218 324.723	131.0	8.26(−4)	11.3	0.65	31(10)	1.5(0.5)	2.8(0.2)
27–26	245 606.320	165.0	1.18(−3)	10.0	0.62	27(10)	0.9(0.2)	2.2(0.1)
28–27	254 699.500	177.3	1.32(−3)	9.7	0.60	20(12)	1.0(0.2)	1.1(0.1)
DC_3N								
9–8	75 987.138	18.2	3.39(−5)	32.4	0.86	26(6)	2.7(1.3)	1.8(0.5)
10–9	84 429.814	22.3	4.67(−5)	29.8	0.85	29(6)	2.0(0.7)	2.5(0.3)
11–10	92 872.375	26.7	6.24(−5)	26.4	0.84	25(4)	1.8(0.3)	2.9(0.1)
13–12	109 757.133	36.9	1.04(−4)	22.4	0.83	31(11)	1.9(1.2)	2.1(0.5)
18–17	151 966.372	69.3	2.78(−4)	16.2	0.77	19(3)	1.3(0.2)	0.4(0.1)
HC_5N								
31–30	82 539.039	63.4	6.04(−5)	29.8	0.85	36(8)	1.5(0.5)	3.5(0.2)
32–31	85 201.346	67.5	6.64(−5)	28.9	0.85	27(5)	2.0(0.7)	2.5(0.3)
34–33	90 525.889	76.0	7.98(−5)	27.2	0.85	14(2)	1.7(0.4)	2.4(0.2)
40–39	106 498.910	104.8	1.30(−4)	23.1	0.84	13(2)	1.3(0.1)	2.5(0.1)

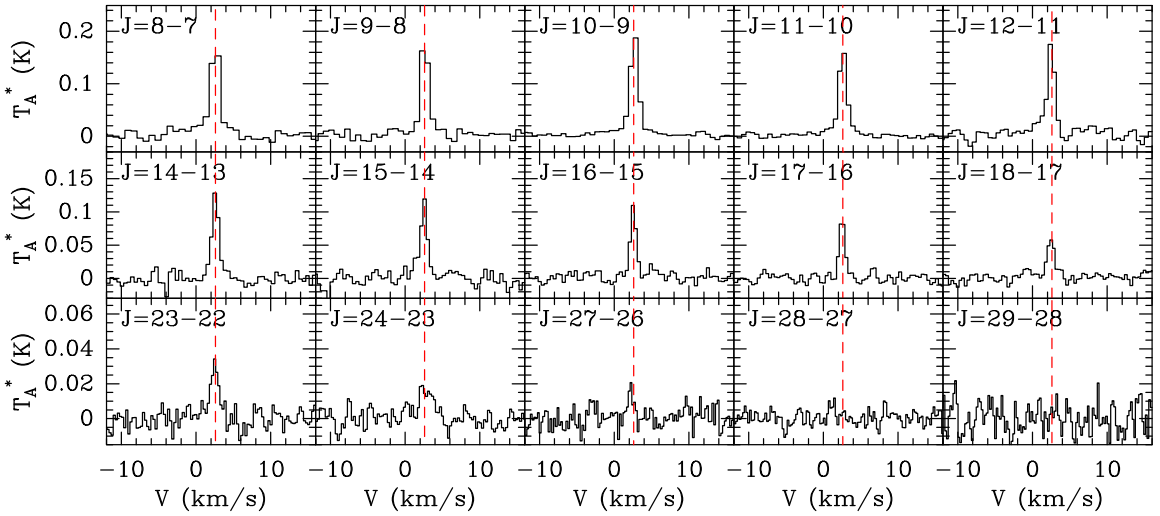

Figure A1. Montage of some HC_3N lines detected towards L1157-mm.

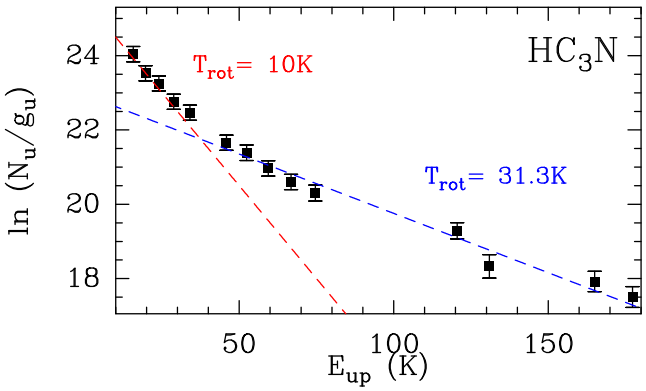

Figure A2. Rotational diagram analysis of HC_3N lines detected towards L1157-mm. The emission was corrected for the coupling between the source and the telescope beam assuming a typical size of 20 arcsec for the protostellar envelope. The fits to the two physical components accounting for the emission are shown in red and blue, respectively. In red, the cold component at $T_{\rm rot} = 10.0 \pm 0.3$ K and $N(HC_3N) = (5.3 \pm 0.6) \times 10^{12}$ cm^{-2}; in blue, the warmer component at $T_{\rm rot} = 31.3 \pm 1.2$ K and $N(HC_3N) = (7.2 \pm 1.0) \times 10^{12}$ cm^{-2}.

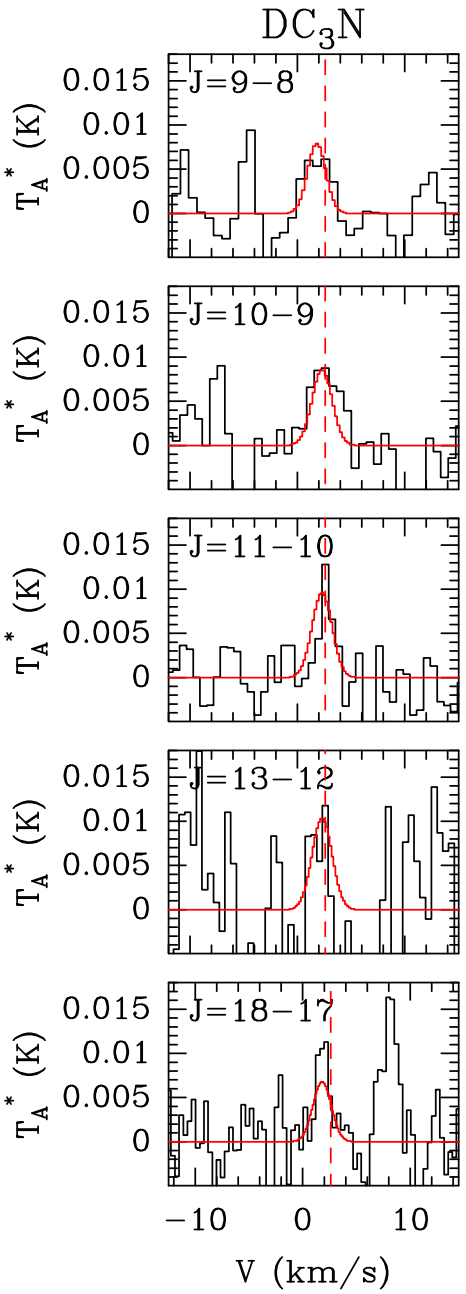

Figure A3. Montage of some DC_3N lines detected towards L1157-mm. We have superposed in red the best LTE fit to the emission with $T_{rot} = 22.5 \pm 1.6$ K and $N(DC_3N) = (3.4 \pm 0.5) \times 10^{11}$ cm^{-2} and a source size of 20 arcsec.

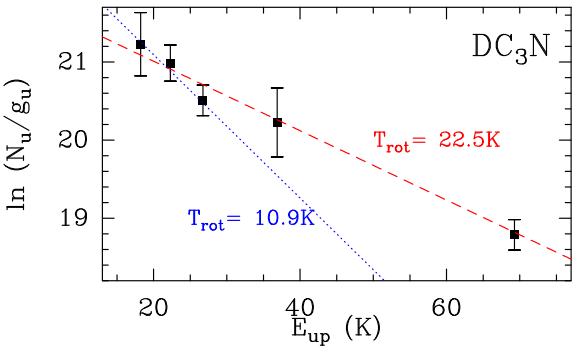

Figure A4. Rotational diagram analysis of DC_3N emission. The emission was corrected for the coupling between the source and the telescope beam assuming a typical size of 20 arcsec. The best fit (dashed red line) is obtained for $T_{rot} = 22.5 \pm 1.6$ K and $N(DC_3N) = (3.4 \pm 0.5) \times 10^{11}$ cm^{-2}. The fit obtained when considering only the data in the $E_{up} < 40$ K range yields $T_{rot} = 10.9 \pm 1.7$ K and $N(DC_3N) = (5.2 \pm 1.8) \times 10^{11}$ cm^{-2}; it is drawn by the blue dotted line.

This paper has been typeset from a TEX/LATEX file prepared by the author.